

Full Characterization of the Mechanical Properties of 11–50 nm Ultrathin Films: Influence of Network Connectivity on the Poisson's Ratio

Jorge N. Hernandez-Charpak,^{*,†,‡} Kathleen M. Hoogeboom-Pot,^{†,‡} Qing Li,[†] Travis D. Frazer,[†] Joshua L. Knobloch,[†] Marie Tripp,[‡] Sean W. King,[‡] Erik H. Anderson,[§] Weilun Chao,[§] Margaret M. Murnane,[†] Henry C. Kapteyn,[†] and Damiano Nardi^{†,‡}

[†]JILA and Department of Physics, University of Colorado, Boulder, Colorado 80309-0440, United States

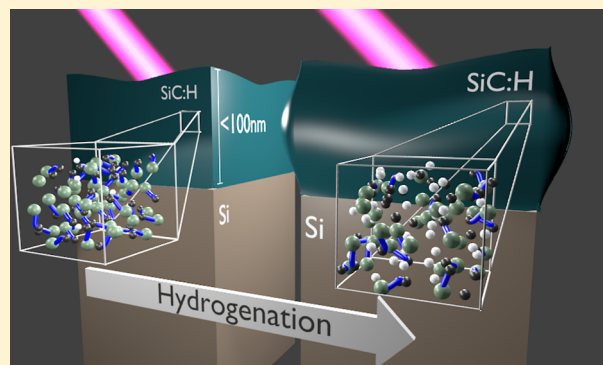
[‡]Intel Corp., 2501 NW 229th Avenue, Hillsboro, Oregon 97124, United States

[§]Center for X-ray Optics, Lawrence Berkeley National Laboratory, Berkeley, California 94720, United States

S Supporting Information

ABSTRACT: Precise characterization of the mechanical properties of ultrathin films is of paramount importance for both a fundamental understanding of nanoscale materials and for continued scaling and improvement of nanotechnology. In this work, we use coherent extreme ultraviolet beams to characterize the full elastic tensor of isotropic ultrathin films down to 11 nm in thickness. We simultaneously extract the Young's modulus and Poisson's ratio of low-*k* a-SiC:H films with varying degrees of hardness and average network connectivity in a single measurement. Contrary to past assumptions, we find that the Poisson's ratio of such films is not constant but rather can significantly increase from 0.25 to >0.4 for a network connectivity below a critical value of ~ 2.5 . Physically, the strong hydrogenation required to decrease the dielectric constant *k* results in bond breaking, lowering the network connectivity, and Young's modulus of the material but also decreases the compressibility of the film. This new understanding of ultrathin films demonstrates that coherent EUV beams present a new nanometrology capability that can probe a wide range of novel complex materials not accessible using traditional approaches.

KEYWORDS: Ultrafast X-rays, nanometrology, nanomechanical properties, ultrathin films, photoacoustics



A broad range of materials science and nanotechnology relies on the fabrication of ultrathin films that can now be deposited with single-atom layer precision. However, nanoscale characterization techniques have not yet reached comparable precision.¹ Accurate characterization of ultrathin films and nanostructures not only enables the design, manufacture, and process control of nanoscale devices but is also critical for understanding the physics of nanoscale systems, for example, how elastic properties change with film thickness, doping, or structural changes.^{2–4}

While a number of techniques are available for the mechanical characterization of thin films, they become less accurate as the film thickness shrinks below 100 nm. Contact techniques such as nanoindentation struggle to decouple the properties of the substrate from those of the film for thicknesses below 1 μm . Moreover, reliable measurements of films with thicknesses of hundreds of nanometers is only possible by using complex modeling.^{5,6} Noncontact techniques can be used successfully for sub-1 μm films but still face various challenges. Brillouin light scattering techniques rely on the study of the interaction of light and acoustic phonons and can

ideally extract the full elastic tensor of a material. When the acoustic impedance between the film and the substrate is large, Brillouin light scattering has been used to successfully characterize the full elastic tensor of a 25 nm thin film.⁷ However, in the majority of cases, interpretation of the experimental data requires complex modeling, making it difficult to extend this approach to sub-100 nm thin films. Moreover, the weak intensity of the scattered light, combined with the challenge of properly identifying the phonon modes, make this approach strongly dependent on the experimental accuracy attained.⁸ Picosecond ultrasonics, another powerful noncontact technique, utilizes visible light to probe the propagation of acoustic waves in materials launched either by a train of short laser pulses or by the impulsive excitation of metallic transducers on a surface.^{9–14} This technique is intrinsically limited by the wavelength of visible light to

Received: November 6, 2016

Revised: February 17, 2017

Published: February 27, 2017



probing surface acoustic waves (SAWs) with wavelengths of hundreds of nanometers or greater. This makes it difficult to extract the full elastic tensor of films <150 nm in thickness.¹³ Nevertheless, due to the simplicity of the data analysis, this approach is attractive for characterizing the Young's modulus of films down to 5 nm in thickness,¹² provided that a value for the Poisson's ratio can be assumed. However, as we show here, this is not always a correct assumption.

Fortunately, laser-like beams at very short wavelengths can now be routinely generated using high harmonic generation (HHG) up-conversion of femtosecond lasers. These new quantum light sources are providing powerful new tools for probing and understanding nanoscale material properties and function. The short wavelengths of extreme ultraviolet (EUV) beams are sensitive to picometer-scale displacements of a surface, while the femtosecond duration of HHG pulses is fast enough to capture thermal and acoustic dynamics in few-nanometer-scale structures. Recent work using coherent HHG beams has uncovered new nanoscale materials properties, including how thermal transport changes dramatically at dimensions on the order of the phonon mean free path^{15,16} and how the mechanical properties of sub-5 nm films dramatically change from bulk, even when the density does not.⁴

Here, we use the exquisite sensitivity and stability of short-wavelength coherent EUV high harmonic beams to characterize the full elastic tensor of isotropic low-*k* dielectric films down to 11 nm in thickness for the first time. We simultaneously extract the Young's modulus and Poisson's ratio of low-*k* a-SiC:H dielectric films on silicon substrate with varying degrees of hardness in a single measurement with Young's modulus ranging from 5 to 197 GPa and average network connectivity from 2.1 to 3.2. The characterized Young's modulus values are in excellent agreement with measurements using alternate techniques on the same materials.¹⁷ However, contrary to past assumptions, the Poisson's ratio of such films is not constant but rather increases significantly from 0.25 to 0.45 for films with Young's modulus in the range of 5–30 GPa. These films have an average network connectivity below a value of 2.5, showing for the first time that the network connectivity can significantly affect the Poisson's ratio in these materials.

This result can be understood within the framework of topological constraint theory developed by Phillips and Thorpe¹⁸ and presented by Mauro.¹⁹ In this model, the flexibility and stress of the material can be understood by how constrained the atoms are in the network. The average number of atomic constraints *n* in a material has to be ≥3 for a material to be rigid and <3 for it to be flexible. The average number of atomic constraints is related to the average network connectivity (or average coordination of atoms) $\langle r \rangle$ by the relation

$$n = \frac{\langle r \rangle}{2} + (2\langle r \rangle - 3) \quad (1)$$

Using this relationship, setting *n* to 3 the critical value at zero-temperature of the network connectivity is found to be $\langle r \rangle = 2.4$, which is referred to as the rigidity percolation threshold. The increase in Poisson's ratio observed is a direct consequence of the hydrogenation of the material that was required in order to tailor the dielectric constant. Films that have undergone extensive hydrogenation will have more broken bonds, which decreases the network connectivity in the material to below the rigidity percolation threshold. The successful extraction of the

full elastic tensor of an isotropic 11 nm film in combination with uncovering a previously unknown trend in the Poisson's ratio, demonstrates that EUV nanometrology can probe a wide range of novel complex materials to extract new information that could not be accessed using existing traditional approaches.

In our experiment, we extend concepts from picosecond ultrasonics into the deep nanoregime by using shorter wavelength coherent beams (see Figure 1). For our measure-

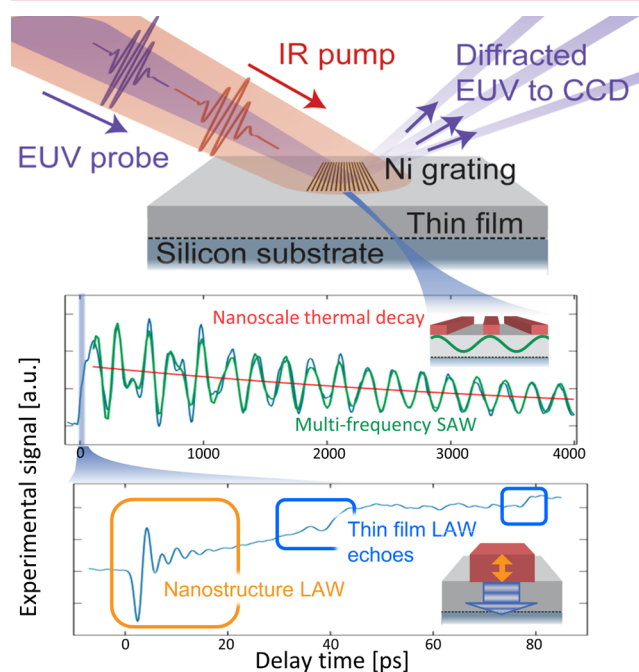


Figure 1. Experimental setup. An array of Ni nanolines is excited using a near-IR ultrashort pump pulse. The surface dynamics are probed at a later time by diffracting a coherent EUV beam from the laser-heated sample (top). Multiple physical phenomena are tracked through the change in diffraction signal (bottom). First, on picosecond time scales the resonant vertical breathing mode of the nanowires is visible (yellow), as well as the echoes from longitudinal acoustic waves launched into the film that reflect from the film–substrate interface (blue). On nanosecond time scales, the SAWs dynamics (green) are superimposed on the thermal decay of the Ni nanowires as the energy dissipates into the film and substrate (red). Note that the data trace shown here from our past foundational work is for illustration purposes only.²³

ments, periodic gratings of nickel nanolines are deposited onto thin film samples with periods *P* varying from 45 to 1500 nm and with a constant filling fraction of one-third. Each grating covers a total film area of 150 μm by 150 μm. The pump laser beam consists of 30 fs duration pulses at a wavelength of 780 nm that irradiate the sample at a fluence of ~10 μJ/pulse in a 400 μm diameter spot size to ensure a nearly uniform heating of the full Ni grating area. The small height (~12 nm on average) of the nanolines ensures a nearly uniform heating of the individual grating lines. Upon heating, the metallic nanostructures expand impulsively and launch acoustic waves: SAWs in the film and substrate, and longitudinal acoustic waves (LAWs) within the nanostructures and also within the film and substrate. The first order SAW wavelength Λ is set by the period of the nanostructures that for the 45 nm grating period represents SAW wavelengths that are as small as previous record setting work²⁰ and an order of magnitude shorter than

those accessible using current visible transient grating techniques.^{21,22}

Detection of the shortest-wavelength SAWs requires short-wavelength probe light with a wavelength comparable to the SAW period. To generate an EUV high harmonic probe beam, we focus high intensity (2 mJ) short pulses (<25 fs) from a Ti:sapphire laser at a wavelength of 780 nm into a hollow-core waveguide filled with argon gas at pressures around 30 Torr.^{24,25} As the intense laser field ionizes the atoms, the electrons are driven nonlinearly, creating a nanoscale dipole quantum antenna that emits high-order harmonics of the driving laser.²⁶ When properly phase matched so that the emission from many atoms adds coherently to form a laser-like beam,^{24,25} 3–5 harmonic orders are efficiently produced (25th–29th orders) at wavelengths around 30 nm. The HHG probe beam is then focused by a glancing-incidence toroidal mirror onto the sample with a spot size of ~100 μm diameter and ~2 nJ per pulse (see Figure 1 top). The EUV HHG probe beam then diffracts from the dynamically changing nanostructured surface and reflected light is captured on an EUV-sensitive CCD camera. The diffraction of such short-wavelength light offers exceptional phase sensitivity to surface deformations as small as tens of picometers.^{15,16,22} Furthermore, the very short penetration depth of the EUV beam and lack of sensitivity to small changes in electron densities and electronic excitations induced by the IR pump beam ensure that the diffracted EUV signal is sensitive exclusively to the changing spatial profile of the surface.

By monitoring the EUV diffraction as a function of delay time between the laser pump and EUV probe pulses, we can simultaneously resolve the different acoustic and thermal dynamics of the sample, as illustrated in Figure 1 bottom. Resonant LAWs are launched in the metallic nanostructures with few picosecond periods and lifetimes. ~5–50 ps echoes can be seen from LAWs propagating down into the film and reflecting off the substrate interface; ~100 ps period SAWs are launched at the same time; finally, one can observe the nanosecond-scale thermal decay of the nanolines as heat dissipates into the film and substrate. For sufficiently short nanostructure periods, the SAW is mostly confined in the thin film, and thus we can extract the LAW and SAW velocities, which are exquisitely sensitive to the elastic properties of the films. The LAW and SAW velocities, v_{LAW} and v_{SAW} are given by

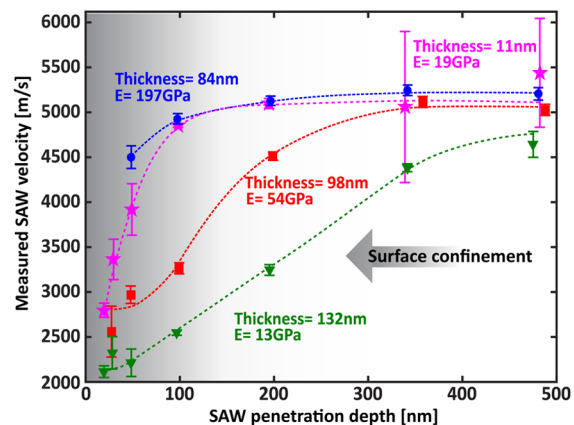
$$v_{\text{LAW}} = \frac{d}{t_{\text{echo}}} \quad (2)$$

$$v_{\text{SAW}} = \Lambda f_{\text{SAW}} \quad (3)$$

where d is the thickness of the thin film material obtained through X-ray reflectivity (XRR) measurements, t_{echo} is the measured round-trip time between LAW echoes at the surface, and f_{SAW} is the measured SAW frequency.

We note that we are able to detect the LAW reflection echoes even from interfaces with low acoustic impedance mismatch (less than 20%) due to the exceptional sensitivity of our probe. In addition, the SAW wavelength Λ is set by the periodicity of the gratings, and the SAW penetration depth is directly related to this period $\zeta \approx \Lambda/\pi$.^{27,28} Therefore, by performing measurements on each film with different grating periodicities, we selectively probe different depths into the sample, as demonstrated by the experimentally extracted v_{SAW} values shown in Figure 2a. This selectivity allows us to probe

a. Experimental data



b. Simulated data

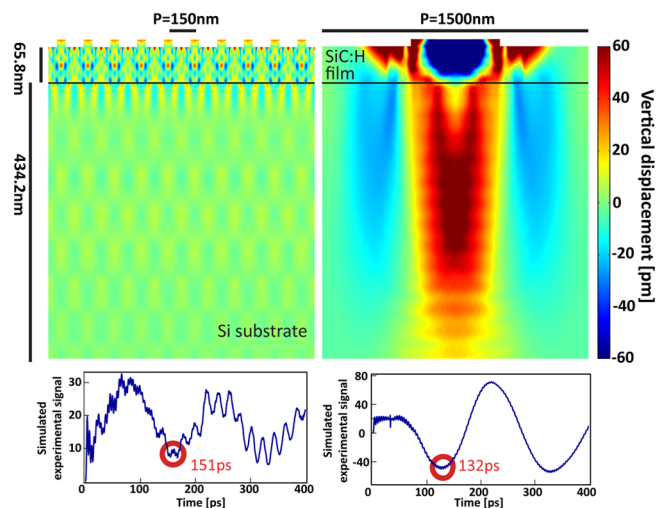


Figure 2. (a) Measured SAW velocity for three different thin film samples and different SAW penetration depths set by grating periodicity. Large penetration SAWs are mostly sensitive to the material properties of the substrate and are comparable for different samples. Small SAW penetration depths confine the SAW and are exclusively sensitive to the thin film properties. SAW velocities are also lower for softer films (green triangles and red squares and pink stars) than for stiffer ones (blue dots), as expected. Dashed lines are guides to the eye. (b) Simulated displacement field from an FEA simulation for a 65.8 nm thin film. SAWs generated for a 150 nm periodicity grating are fully confined in the thin film material (left), whereas SAWs generated from a 1500 nm periodicity grating penetrate the substrate material (right). Both simulated data sets correspond to the first-SAW minimum for that grating, as shown on the simulated experimental signal below for reference.

either the elastic properties of the silicon substrate for large grating periodicities or the ultrathin film for very small grating periodicities, as well as following the transition from one regime to the other as illustrated in Figure 2b. Note, as might be expected, that the transition between v_{SAW} corresponding to near full confinement in the thin film to v_{SAW} corresponding to bulk is more abrupt for thin film (pink stars) compared with thicker films (green triangles, blue circles, and red squares). The film properties relevant for the data analysis can be found in the Supporting Information.

By extracting the velocities of the acoustic waves excited by the smallest gratings, we can calculate the elastic constants of the films using

$$c_{11} = \rho(v_{\text{LAW}})^2 \quad (4)$$

$$c_{44} = \rho \left(\frac{v_{\text{SAW}}}{\xi} \right)^2 \quad (5)$$

where ρ is density of the thin film material obtained through XRR measurements, ξ is the ratio between SAW velocity and bulk transverse wave velocity,²⁹ and c_{11} and c_{44} are the independent components of the elastic tensor. However, it is more intuitive to work with Young's modulus E and Poisson's ratio ν , which are related to c_{11} and c_{44} of an isotropic material as follows³⁰

$$E = c_{44} \frac{3c_{11} - 4c_{44}}{c_{11} - c_{44}} \quad (6)$$

$$\nu = \frac{c_{11} - 2c_{44}}{2(c_{11} - c_{44})} \quad (7)$$

The measured LAW velocity can be used to directly extract the c_{11} elastic constant of the film. For the measured SAW velocity, the presence of the deposited nanostructures introduces a small mass loading on the film that shifts the SAW frequency from the intrinsic value, introducing a systematic error in eq 2. This mass loading effect is different for each of our grating geometries and shifts the measured SAW velocity by different amounts for each grating periods. In order to correct for this shift, we extend the procedure developed by Nardi et al.^{28,29} to periodic nickel nanostructures on thin films deposited on a silicon substrate. The details of our modeling are presented in the [Supporting Information](#). We performed the finite element analysis (FEA) calculations using the commercial software COMSOL Multiphysics for the geometry of our samples (verified through atomic force microscopy and scanning electron microscopy measurements) to extract the eigenfrequencies of the system in the presence of nanostructures. We match these calculations to the measured SAW frequencies of our different grating periods by varying the elastic constants of the film material while keeping c_{11} constant to the measured value. This allows us to successfully eliminate the influence of mass loading on our measurements and extract a value for c_{44} . The experimental error bars presented in this work represent the totality of the parameter space that can reproduce the experimental results within error bars, regardless of the probability. The error bars are calculated by matching the elastic properties to all of the limiting error bar values of the relevant parameters and experimental data, this includes f_{SAW} , t_{echo} , ρ , and d .

Using this method, we simultaneously extract the Young's modulus and Poisson's ratio of a series of 66–132 nm isotropic low- k dielectric thin films, as shown in [Figure 3](#). Our extracted Young's modulus agrees well with previous measurements on the same films using state of the art nanoindentation.¹⁷ However, we observe a previously unknown trend in the Poisson's ratio of these materials with decreasing Young's modulus. In contrast to previous studies where Poisson's ratio was thought to be constant in this type of material,¹⁷ we find that this assumption is not correct for soft films with Young's modulus lower than 30 GPa. Interestingly, although the nanoindentation measurements assume a constant Poisson's ratio, our extracted Young's modulus values agree well across

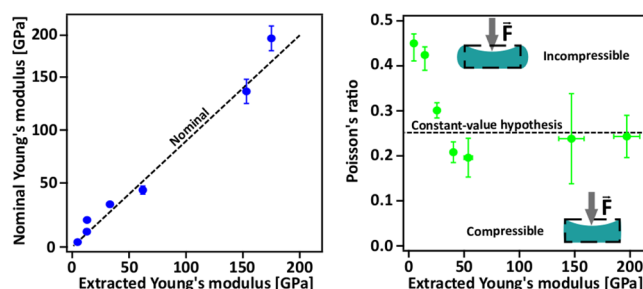


Figure 3. Extracted Young's modulus (left) and Poisson's ratio (right) of a series of SiC:H thin films. The extracted Young's modulus (blue) shows good agreement with nominal values, comparable with the results from King et al.¹⁷ This is the first time that the Poisson's ratio (green) for a sub-100 nm isotropic thin film series has been characterized. While the extracted values are consistent with a constant-value hypothesis for films with Young's modulus >40 GPa, for films with lower Young's modulus, the Poisson's ratio increases significantly. A Poisson's ratio of 0 corresponds to a compressible material, whereas a Poisson's ratio of 0.5 corresponds to an incompressible material, shown schematically.

the whole range. This demonstrates that nanoindentation is inherently insensitive to the Poisson's ratio of the material.

Physically, the Poisson's ratio of these materials is related to the average network connectivity, as are other thermal and elastic parameters.¹⁷ In the process of hydrogenation to lower the film's dielectric constant k , atomic bonds are broken in the lattice. With enough hydrogenation, the average network connectivity will eventually land below the rigidity percolation threshold of ~ 2.5 . The average network connectivity for these samples was extracted from nuclear reaction analysis and Rutherford backscattering measurements detailed in refs 31 and 17. From these measurements, the value of $\langle r \rangle$ was obtained by adding up the measured mole fractions of each element to its typical coordination number (i.e., $\langle r \rangle_{\text{Si}} = 4$, $\langle r \rangle_{\text{C}} = 4$, $\langle r \rangle_{\text{O}} = 2$, $\langle r \rangle_{\text{H}} = 1$). With this information, King et al.¹⁷ observed large changes in several elastic and thermal properties of isotropic SiC:H films below a rigidity percolation threshold of 2.5. Here we observe that the Poisson's ratio also changes, increasing to values as high as 0.455, causing the film to behave like an incompressible material, similar to a polymer or water as shown in [Figure 4](#). This is consistent with observations from Matsuda et al.³² of an increase of the flexibility of similar materials below the critical value of network connectivity of 2.44. Moreover,

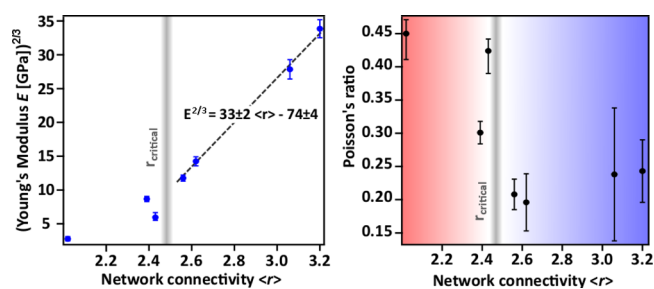


Figure 4. Measured Young's modulus E values (blue, left) and Poisson's ratio values (black, right) for the film series as a function of the average bond coordination, $\langle r \rangle$. The extracted Young's modulus values yield the same average network connectivity dependence as King et al.¹⁷ for $\langle r \rangle$ values above a critical value of $r_{\text{critical}} \approx 2.5$. This same critical value of r_{critical} marks the deviation of Poisson's ratio from the assumed constant value.

using the model presented by Cao and Li³³ to classify metallic glass materials in ductile and brittle categories we see that this series of isotropic SiC:H films go through a transition from brittle to ductile as the average network connectivity is reduced past the critical value.

In addition to studying a series of hydrogenated SiC:H thin films of varying hardness, we also extracted the Young's modulus and Poisson's ratio of a 10.9 nm SiOC:H isotropic thin film deposited on a silicon substrate. Its nominal Young's modulus value of 20 GPa was obtained at Intel Corp. through nanoindentation measurements of a 500 nm thick film of the same material. We performed this new measurement to explore the limits of EUV acoustic metrology, using gratings with periods as small as 60 nm to launch SAWs that were mostly confined to the thin film material (i.e., where the first-order SAW penetration depth was ~ 19 nm). By applying our analysis procedure, assuming a smooth, ideal interface, we were able to successfully reproduce the observed acoustic dynamics in our simulations and extract values for both Poisson's ratio and Young's modulus. Although uncertainty due to incomplete confinement of the first order SAW in the thin film contributes to larger error bars on our data, when combined with precise finite element simulations we can still extract reliable measurements for Young's modulus and a reasonable estimate for Poisson's ratio. The extracted value for the Young's modulus is 35 GPa (error bars extending from 26 to 54 GPa). This is slightly larger than the 20 GPa value measured on a thick film of the same material, which could be due to thickness-determined changes in the elastic properties of the material when deposited at this extremely small thickness.⁴ The extracted Poisson's ratio has an exact fit to experimental measurements at 0.393, but has a large allowed range (0–0.450) within experimental uncertainty. This large uncertainty in the Poisson's ratio stems from the fact that the return time of the LAWs reflected from the film–substrate interface is very short (3.11 ps) compared with our experimental error on its measurement mostly due to LAW pulse duration (± 500 fs). Future upgrades to our system will allow us to overcome this limitation and enable probing of thickness-dependent mechanical properties in ultrathin films.

We also considered the potential impact of a thin layer of SiO₂ at the film–substrate interface, potentially introduced during the fabrication process and undetected by the characterization procedures. We found that accounting for a 1 nm-thick oxide layer in our data analysis procedures results in a shift in the extracted Young's modulus range to higher values by less than 5% and less than 13% for a 2 nm-thick one. Therefore, the existence of this oxide would not explain the discrepancy between the ultrathin film Young's modulus and the 500 nm thin film nanoindentation measurement. This uncertainty could be significantly reduced in the future with the development of coherent EUV reflectometry to characterize our samples. Our measurement represents a full characterization of the elastic properties of the thinnest film to date, including metallic films.⁷ Moreover, our approach is not yet limited by the probe light source but rather by the nanofabrication that dictates the SAW wavelength. In the future, by using physical gratings with even smaller period and EUV transient grating excitation it will be possible to fully characterize sub-10 nm films, explore size-dependent anisotropies, and asymmetries in the elastic tensor.³⁴

In conclusion, we demonstrate that coherent EUV nanometrology can simultaneously characterize the Young's

modulus and Poisson's ratio of isotropic sub-100 nm thin films on substrates. This technique allows selective depth sensitivity by tailoring the geometry of a nanopatterned transducer on the film surface. We demonstrated the robustness and reliability of EUV nanometrology by fully characterizing a series of isotropic a-SiC:H low-*k* dielectric 66–132 nm thin films, which revealed they behave as incompressible polymer materials once the average network connectivity is below a critical value of $\langle r \rangle \approx 2.5$. This new insight shows how coherent EUV nanometrology can impact the understanding, design, and utilization of ultrathin films in nanoelectronic devices. Finally, we also demonstrated a new milestone by extracting a full elastic tensor of a 10.9 nm SiOC:H isotropic film on silicon, which represents the thinnest film fully characterized to date.

■ ASSOCIATED CONTENT

Supporting Information

The Supporting Information is available free of charge on the ACS Publications website at DOI: [10.1021/acs.nanolett.6b04635](https://doi.org/10.1021/acs.nanolett.6b04635).

Sample characterization, data analysis methods, tables, figure, and additional references (PDF)

■ AUTHOR INFORMATION

Corresponding Author

*E-mail: Jorge.hernandez@jila.colorado.edu.

ORCID

Jorge N. Hernandez-Charpak: [0000-0003-3296-6929](https://orcid.org/0000-0003-3296-6929)

Author Contributions

J.N.H.C. and K.M.H.-P. contributed equally.

Notes

The authors declare no competing financial interest.

■ ACKNOWLEDGMENTS

We gratefully acknowledge support from the U.S. Department of Energy Atomic, Molecular, and Optical Sciences Program Award No. FG02-99ER14982, and a Gordon and Betty Moore Foundation EPiQS Award through Grant GBMF4538.

■ REFERENCES

- (1) King, S. W.; Simka, H.; Herr, D.; Akinaga, H.; Garner, M. Research Updates: The three M's (materials, metrology, and modeling) together pave the path to future nanoelectronic technologies. *APL Mater.* **2013**, *1*, 040701.
- (2) Fedorchenko, A. I.; Wang, A.; Cheng, H. H. Thickness dependence of nanofilm elastic modulus. *Appl. Phys. Lett.* **2009**, *94*, 152111.
- (3) Gong, B.; Chen, Q.; Wang, D. Molecular dynamics study on size-dependent elastic properties of silicon nanoplates. *Mater. Lett.* **2012**, *67*, 165–168.
- (4) Hoogeboom-Pot, K.; Turgut, E.; Hernandez-Charpak, J. N.; Shaw, J. M.; Kapteyn, H. C.; Murnane, M. M.; Nardi, D. Nondestructive Measurement of the Evolution of Layer-Specific Mechanical Properties in Sub-10 nm Bilayer Films. *Nano Lett.* **2016**, *16*, 4773–4778.
- (5) Hay, J.; Crawford, B. Measuring substrate-independent modulus of thin films. *J. Mater. Res.* **2011**, *26*, 727–738.
- (6) Zhou, B.; Prorok, B. C. A new paradigm in thin film indentation. *J. Mater. Res.* **2010**, *25*, 1671.
- (7) Zizka, J.; King, S.; Every, A. G.; Sooryakumar, R. Mechanical properties of low- and high-*k* dielectric thin films: A surface Brillouin light scattering study. *J. Appl. Phys.* **2016**, *119*, 144102.

- (8) Link, A.; Sooryakumar, R.; Bandhu, R. S.; Antonelli, G. A. Brillouin light scattering studies of the mechanical properties of ultrathin low-k dielectric films. *J. Appl. Phys.* **2006**, *100*, 013507.
- (9) Thomsen, C.; Grah, H. T.; Maris, J. H.; Tauc, J. Picosecond interferometric technique for study of phonons in the Brillouin frequency range. *Opt. Commun.* **1986**, *60*, 55–58.
- (10) Grah, H. T.; Maris, H. J.; Tauc, J. Picosecond ultrasonics. *IEEE J. Quantum Electron.* **1989**, *25*, 2562–2569.
- (11) Matsuda, O.; Larciprete, M. C.; Li Voti, R.; Wright, O. B. Fundamentals of picosecond laser ultrasonics. *Ultrasonics* **2015**, *56*, 3–20.
- (12) Ogi, H.; Fujii, M.; Nakamura, N.; Shagawa, T.; Hirao, M. Resonance acoustic-phonon spectroscopy for studying elasticity of ultrathin films. *Appl. Phys. Lett.* **2007**, *90*, 191906.
- (13) Mante, P. A.; Robillard, J. F.; Devos, A. Complete thin film mechanical characterization using picosecond ultrasonics and nanostructured transducers: experimental demonstration on SiO₂. *Appl. Phys. Lett.* **2008**, *93*, 071909.
- (14) Devos, A.; Robillard, J. F.; Côte, R.; Emery, P. High-laser-wavelength sensitivity of the picosecond ultrasonic response in transparent thin films. *Phys. Rev. B: Condens. Matter Mater. Phys.* **2006**, *74*, 064114.
- (15) Siemens, M. E.; Li, Q.; Yang, R.; Nelson, K. A.; Anderson, E. H.; Murnane, M. M.; Kapteyn, H. C. Quasi-ballistic thermal transport from nanoscale interfaces observed using ultrafast coherent soft X-ray beams. *Nat. Mater.* **2010**, *9*, 26–30.
- (16) Hoogeboom-Pot, K. M.; Hernandez-Charpak, J. N.; Gu, X.; Frazer, T. D.; Anderson, E. H.; Chao, W.; Nardi, D. A new regime of nanoscale thermal transport: Collective diffusion increases dissipation efficiency. *Proc. Natl. Acad. Sci. U. S. A.* **2015**, *112*, 4846–4851.
- (17) King, S. W.; Bielefeld, J.; Xu, G.; Lanford, W. A.; Matsuda, Y.; Dauskardt, R. H.; Gidley, D. Influence of network bond percolation on the thermal, mechanical, electrical and optical properties of high and low-k a-SiC:H thin films. *J. Non-Cryst. Solids* **2013**, *379*, 67–79.
- (18) Phillips, J. C.; Thorpe, M. F. Constraint theory, vector percolation and glass formation. *Solid State Commun.* **1985**, *53*, 699–702.
- (19) Mauro, J. C. Topological constraint theory of glass. *American ceramic society bulletin* **2011**, *90*, 31–37.
- (20) Li, Q.; Hoogeboom-Pot, K.; Nardi, D.; Murnane, M. M.; Kapteyn, H. C.; Siemens, M. E.; Anderson, E. H.; Hellwig, O.; Dobisz, E.; Gurney, B.; Yang, R.; Nelson, K. A. Generation and control of ultrashort-wavelength two-dimensional surface acoustic waves at nanoscale interfaces. *Phys. Rev. B: Condens. Matter Mater. Phys.* **2012**, *85*, 195431.
- (21) Johnson, J. A.; Maznev, A. A.; Cuffe, J.; Eliason, J. K.; Minnich, A. J.; Kehoe, T.; Torres, C.; Sotomayor, M.; Gang, C.; Nelson, K. A. Direct measurement of room-temperature nondiffusive thermal transport over micron distances in a silicon membrane. *Phys. Rev. Lett.* **2013**, *110*, 025901.
- (22) Tobey, R. I.; Siemens, M. E.; Murnane, M. M.; Kapteyn, H. C.; Torchinsky, D. H.; Nelson, K. A. Transient grating measurement of surface acoustic waves in thin metal films with extreme ultraviolet radiation. *Appl. Phys. Lett.* **2006**, *89*, 091108.
- (23) Li, Q.; Hoogeboom-Pot, K.; Nardi, D.; Deeb, C.; King, S.; Tripp, M.; Anderson, E.; Murnane, M. M.; Kapteyn, H. C. Characterization of ultrathin films by laser-induced sub-picosecond photoacoustic with coherent extreme ultraviolet detection. *Proc. SPIE* **2012**, *8324*, 83241P.
- (24) Rundquist, A.; Durfee, C. G.; Chang, Z.; Herne, C.; Backus, S.; Murnane, M. M.; Kapteyn, H. C. Phase-matched generation of coherent soft X-rays. *Science* **1998**, *280*, 1412–1415.
- (25) Bartels, R. A.; Paul, A.; Green, H.; Kapteyn, H. C.; Murnane, M. M.; Backus, S.; Christov, I. P.; Liu, Y.; Attwood, D.; Jacobsen, C. Generation of Spatially Coherent Light at Extreme Ultraviolet Wavelengths. *Science* **2002**, *297*, 376–378.
- (26) McPherson, A.; Gibson, G.; Jara, H.; Johann, U.; Lik, T. S.; McIntyre, I. A.; Boyer, K.; Rhodes, C. K. Studies of multiphoton production of vacuum-ultraviolet radiation in the rare gases. *J. Opt. Soc. Am. B* **1987**, *4*, 595–601.
- (27) Nardi, D.; Banfi, F.; Giannetti, C.; Revaz, B.; Ferrini, G.; Parmigiani, F. Pseudosurface acoustic waves in hypersonic surface phononic crystals. *Phys. Rev. B: Condens. Matter Mater. Phys.* **2009**, *80*, 104119.
- (28) Nardi, D.; Travaglini, M.; Siemens, M. E.; Li, Q.; Murnane, M. M.; Kapteyn, H. C.; Ferrini, G.; Parmigiani, F.; Banfi, F. Probing thermomechanics at the nanoscale: Impulsively excited pseudosurface acoustic waves in hypersonic phononic crystals. *Nano Lett.* **2011**, *11*, 4126–4133.
- (29) Landau, L.; Lifshitz, E. *Course of Theoretical Physics, Vol. 7: Theory of Elasticity*. Pergamon Press, 1970; pp 110–112.
- (30) Atanackovic, T. M.; Guran, A. *Theory of elasticity for Scientists and Engineers*; Birkhauser, 2000.
- (31) Lanford, W. A.; Parenti, M.; Nordell, B. J.; Paquette, M. M.; Caruso, A. N.; Mantymäki, M.; Hamalainen, J.; Ritala, M.; Klepper, K. B.; Mikkilainen, V.; Nilsen, O.; Tenhaeff, W.; Dudner, N.; Koh, D.; Banerjee, S. K.; Mays, E.; Bielefeld, J.; King, S. W. Nuclear reaction analysis for H, Li, Be, B, C, N, O, and F with and RBS check. *Nucl. Instrum. Methods Phys. Res., Sect. B* **2016**, *371*, 211–215.
- (32) Matsuda, Y.; Kim, N.; King, S. W.; Bielefeld, J.; Stebbins, J. F.; Dauskardt, H. Tunable plasticity in amorphous silicon carbide films. *ACS Appl. Mater. Interfaces* **2013**, *5*, 7950–7955.
- (33) Cao, J.; Li, F. Critical Poisson's ratio between toughness and brittleness. *Philos. Mag. Lett.* **2016**, *96*, 425–431.
- (34) Burg, J. A.; Dauskardt, R. H. Elastic and thermal expansion asymmetry in dense molecular materials. *Nat. Mater.* **2016**, *15*, 974–980.

Supporting information

Full characterization of the mechanical properties of 11-50nm ultrathin films: influence of network connectivity on the Poisson's ratio

Jorge N. Hernandez-Charpak^{1†}, Kathleen M. Hoogeboom-Pot^{1†}, Qing Li¹, Travis D. Frazer¹, Joshua L. Knobloch¹, Marie Tripp², Sean King², Erik H. Anderson³, Weilun Chao³, Margaret M. Murnane¹, Henry C. Kapteyn¹, and Damiano Nardi¹*

¹ JILA and Department of Physics, University of Colorado, Boulder, Colorado 80309-0440, USA

² Intel Corp. 2501 NW 229th Ave, Hillsboro, OR, 97124

³ Center for X-Ray Optics, Lawrence Berkeley National Laboratory, Berkeley, CA 94720

KEYWORDS: Ultrafast X-rays, nanometrology, nano-mechanical properties, ultrathin films, photoacoustics.

**Jorge.hernandez@jila.colorado.edu*

[†]Both authors contributed equally

1. Sample characterization

The thin film samples were provided by Intel Corporation. The Ni nano-grating patterns were deposited at LBNL using e-beam lithography and lift-off. The geometry of the periodic nanolines grating (height, linewidth, height) was characterized using an AFM (Fig. S1 1a,b), with additional SEM measurements taken at LBNL after decoration with a thin Al layer (Fig. S1. 1c).

The thin film thicknesses and densities were characterized through XRR measurements at Intel Corp. These values as well as other film properties are given in table S1.

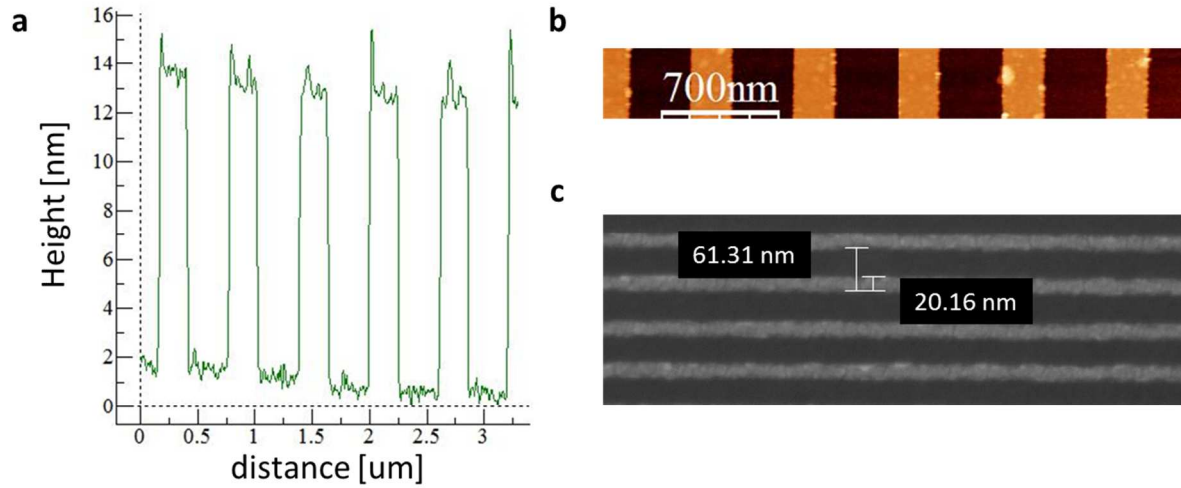


Figure S1. Nanoline grating geometry characterization. a) AFM acquired Height profile of a typical nanowire grating. b) AFM 2D map of a 350nm linewidth grating. c) SEM 2D map of a 20nm linewidth grating.

Nominal thickness [Å]	Measured thickness [Å]	Nominal Young's modulus [GPa]	Wafer #	Network connectivity	C/Si ratio	Density [kg/m ³]
1000	658	4.7	63	2.02	1.10	1300
1000	1031.6	13.05	7	2.39	1.20	1900
1000	1316.2	12.87	5	2.43	1.50	1800
1000	952.5	33.12	75	2.56	1.10	1800
1000	979.1	62.08	65	2.62	1.10	1900
1000	1033	153	9	3.06	0.98	2200
1000	836.4	175	49	3.2	1.02	2700
100	109.1	25	155	N/A	N/A	1500

Table S1. Properties of the SiC:H samples and SiOC:H provided by Intel Corp. used in this work.

2. Data analysis methods

a. Data acquisition and preliminary analysis

On each nanoline grating, several (>5) measurements were performed to ensure the consistency of our data and to reduce error bars. At each pump-probe time delay, we averaged over 50 separate 30ms exposures, with and without the pump pulse incident on the sample. This eliminated the effect of any pulse-to-pulse intensity variations (which are below 10%).

On each time-dependent trace (see Fig. 1 of the main text), we use FFT and Chirp-Z transforms to extract the SAWs frequencies present in the signal, as described in.⁴ We determine the LAW return time by checking for the characteristic signal (as shown in Fig. 1b) in several measurements of different gratings fabricated on the same sample.

The SAW frequencies and LAW return time, together with the grating geometry, are the input for our procedure to account for mass loading effect on the measurement. However, even without accounting for the mass loading, these values still provide the value for the elastic tensor's c_{11} and bound c_{44} by constraining the elastic matrix to be physical.

b. FEA simulations

All simulations were performed using COMSOL Multiphysics software and the data analysis was done in the MATLAB environment. As described in the main text, the two parameters extracted directly from the dynamic diffraction data are: the SAW frequency and the LAW pulse return time. By using the film thickness and density (S.I. table 1), we can directly calculate c_{11} from the LAW pulse return time and provide an estimate of c_{44} . In order to extract an exact value for c_{44} , the mass loading of the nanostructures needs to be accounted for using numerical simulations. We extend the work by Nardi *et al.*²⁵ to include systems with a thin film between the nanostructures and the substrate. Our numerical approach is extremely similar to the procedure outlined in Nardi *et al.*²⁵ for the cases involving a fully confined SAW. The extension of this procedure to account for SAWs propagating in both the thin film and the substrate assumes a perfect interface between the film and substrate. In order to extract the elastic properties of the thin film, simulations of only the largest and smallest gratings are required. In both of these cases, the interface quality has the smallest impact. Nonetheless, the ability of the simulations to reproduce the observed dynamics at all size gratings demonstrates the acceptability of this assumption and the simulation procedure itself. The material properties used for all the studies are listed in table S1 and table S2.

The three main steps of the calculation are as follows.

- i. A time domain simulation to solve the coupled equations for the profiles of T and \mathbf{u} in the time domain for the nanostructure on top of a thin film:

$$\nabla \cdot (\mathbf{c} : \nabla(\mathbf{u} - \alpha \Delta T)) = \rho \frac{\partial^2 \mathbf{u}}{\partial t^2} \quad (\text{S.1})$$

$$\rho C_p \frac{\partial T}{\partial t} + \rho C_p \mathbf{u} \cdot \nabla T = \nabla \cdot (K_{bulk} \nabla T) + Q \quad (\text{S.2})$$

where \mathbf{c} is the elastic tensor, \mathbf{u} is the displacement, ρ is the density of the material, α is the linear coefficient of thermal expansion, T is the temperature, C_p is the specific heat of the material, K_{bulk} is the bulk thermal conductivity and Q is the heat source term accounting for the laser heating of the nano-grating, as described by Banfi *et al.*³² We performed this calculation for the first 100-200 picoseconds (depending on the size of the structure) in order to find the maximum initial deformation of the surface, which is given by the first maximum displacement of the outer corners of the structure. For these calculations, the temperature dynamics are only calculated for the nanostructure, whereas the mechanical dynamics are calculated throughout the system. Therefore, precise knowledge of the thin film thermal properties is not required.

- ii. We perform an eigenfrequency analysis of the grating-film-substrate system to extract the normal modes of the geometry. In this case, COMSOL solves only the mechanical eigenfrequency equation:

$$\rho(f 2 \pi)^2 \mathbf{u} - \nabla \cdot \boldsymbol{\sigma} = \mathbf{F}_V \quad (\text{S.3})$$

where $\boldsymbol{\sigma}$ is the stress of the material, \mathbf{F}_V the load on it, and f the eigenfrequency. The COMSOL solver looks for a solution in a certain range specified by the user.

- iii. Finally, we decompose the displacement field of the time-dependent simulation at the moment of maximum displacement into the normal eigenfrequencies basis. We vary the value of c_{44} around its estimate until the simulated frequencies of the SAWs match those observed in the experiment. The c_{44} at which this match occurs is the true c_{44} of the thin film since COMSOL can account for the perturbation to the SAW velocity caused by the mass loading of the nanostructures.

To calculate the thin film's elastic tensor, first we verify the silicon substrate elastic properties by using these three steps to reproduce the experimental observations at large grating sizes (with approximate film properties given by the experimental results) as the SAW frequency depends largely on the substrate properties at these large penetration depths. Next, we determine the thin film's elastic properties by setting c_{11} to the experimentally extracted value and following the three steps above, sweeping c_{44} to reproduce the experimental results for small grating sizes where the SAW is fully confined to the film material. Lastly, we perform the three steps of calculation on the intermediate grating sizes where the SAWs may be very sensitive to interface effects to verify the validity of our findings. Most of the found values for the intermediate sizes are in good agreement with the experimental values. There are a few discrepancies which are mostly likely due to a complex interface between the thin film and substrate. The simulations on these intermediate grating sizes corroborate the success of our approach and demonstrate that the interface quality is quite good.

Material properties	Nickel	Silicon
C_p , Specific heat (at 300 K) [J/(kg K)]	456.8 ¹⁶	710.0 ³³
K_{bulk} , Bulk thermal conductivity [W/(m K)]	90.9 ³³	149.0 ³⁴
Poisson's ratio	0.31 ¹⁶	N/A
Young's modulus [10^{11} Pa]	2.00 ³⁴	N/A
α , Linear coefficient of thermal expansion [10^{-6} /K]	12.77 ¹⁶	3.00 ³⁶
ρ , Density [kg/m^3]	8910 ¹⁶	2330 ³⁷
(c_{11}, c_{12}, c_{44}) [GPa]	N/A	(165.5, 63.9, 79.5) ³¹

Table S2. Material parameters used in multiphysics simulations.

c. Error bars

Our extraction of SAW frequencies and of LAW return times have error bars inherent to the experimental setup and analysis procedure. For the SAW frequency associated with a particular grating size the error bar is given by the standard deviation of the extracted frequency of different scans. For the LAW return time, the error bar is given by the standard deviation across scans and how short in the signal the signal from the echo is. Note that samples in which the acoustic impedance between film material and silicon is high have much clearer LAW echoes signal and therefore lower error bars.

The final error bar on Young's modulus and Poisson's ratio is determined by propagating the experimental error bars on LAW and SAW measurements through our analysis procedure. As mentioned above, the value for c_{11} can be directly calculated from the experimental measurement of the LAW pulse return time. This value depends on the measured echo return time, density, and thickness of the thin film. There is an error associated with each of these quantities, and thus the error on c_{11} requires independent error propagation using the derivative method,

$$\delta f = \sqrt{\sum_i \left(\frac{\partial f(x_i)}{\partial x_i} \right)^2 (\delta x_i)^2}, \quad (\text{S.4})$$

Where δf is the error on $f(x_i)$, a function of uncorrelated, independent variables x_i each with uncertainty δx_i .

To calculate the error on c_{44} (and thus Young's modulus and Poisson's ratio), the error on density, thickness, and c_{11} must be propagated through the simulation procedure, and the error on the measured SAW frequency must be taken into account. To propagate error through the numerical procedure, we first simulate the value of c_{44} that matches the observed frequency assuming no values have any error. This step yields the data point of Young's modulus and Poisson's ratio quoted in the paper. Next, we alter the values of density, thickness, and c_{11} to the extreme ends of their error bars. We find the combination that achieves the lowest possible SAW frequency for that value of c_{44} . We then account for the error on the measured SAW frequency by increasing the c_{44} value until the simulated SAW frequency matches the extreme upper end of the error bar for the observed experimental SAW frequency. With this procedure, we obtain one end of the error bar for our Young's modulus and Poisson's ratio that we quote in the paper. We do a similar process to calculate the other end of the error bar quoted in the paper, using the parameter values that give the highest possible SAW frequency, and lowering c_{44} to match the lowest end of the experimental SAW frequency error bar. In other words, our error bars on Young's modulus and Poisson's ratio include the most extreme values one could get by choosing any value of an input parameter within the error bars of the measurement. Since the probability is very low that the true value of all of our input values lies at the extreme ends of their error bars, the error bars on our results are very conservative. Even with these very conservative error bars, we were still able to see a very stark trend in the extracted elastic properties. Lastly, it is good to note that the most dominant error came from the error in the measured SAW frequency and LAW echo times.

References:

35. Hopcroft, M. A.; Nix, W. D. ; Kenny, T. W. What is the Young's Modulus of Silicon? *Journal of Microelectromechanical Systems* **2010**, 19, 229-238.
36. Banfi, F.; Pressaco, F.; Revaz, B.; Giannetti, C.; Nardi, D.; Ferrini, G.; Parmigiani, F. *Ab initio* thermodynamics calculation of all-optical time-resolved calorimetry of nanosize systems: Evidence of nanosecond decoupling of electron and phonon temperatures. *Phys. Rev. B* **2010**, 81, 155426.
37. Desai, P. D.; Thermodynamic properties of Iron and Silicon. *J. Phys. Chem. Ref. Data* **15**, 967-983 (1986).
38. Dean, J. A.; *Lange's Handbook of Chemistry* (McGraw-Hill, New York, 15th edition, 1999), pp. 290-294.
39. Zacharias, J.; The temperature dependence of Young's Modulus for Nickel. *Phys. Rev.* **44**, 116-122 (1933).
40. Okada, Y.; Tokumaru, Y. Precise determination of lattice parameter and thermal expansion coefficient of silicon between 300 and 1500 K. *J. Appl. Phys.* **56**, 314-320 (1984).
41. Weber, M. J.; *Handbook of Optical Materials* (CRC Press, Boca Raton, FL, 2003), p. 324.